In situ construction of heteroatom F-doped Mn_3O_4 spinel catalysts with robust activity and SO_2 resistance for NH_3-SCR at low temperature

Chong Chen, Yunxia Wang, Junxi Li, Fengyu Tian, Weijuan Chen, Chao Feng [*], Yuan Pan [*], Yunqi Liu [*]

State Key Laboratory of Heavy Oil Processing, China University of Petroleum, East China, Qingdao 266580, China

ARTICLE INFO

ABSTRACT

Herein, we propose a novel *in situ* construction method of F-doped Mn_3O_4 catalysts through a crystallization-pyrolysis-oxidation strategy. The F-Mn_3O_4-3 % exhibits a NO conversion above 90 % from 150° to 310°C at an ultra-high GHSV of 400,000 h^{-1}. The SO_2 resistance is also significantly improved compared to pure Mn_3O_4. Doping of Mn_3O_4 with F increases the surface acidity and tunes the electronic properties of the catalysts. The increase of acid sites not only facilitates the adsorption of NH_3 species, thereby improving NH_3-SCR activity, but also inhibits SO_2 adsorption on the catalyst surface. The electron conduction between SO_2 and Mn^{3+} can also be effectively inhibited after F replaces O, resulting in the F-doped Mn_3O_4 catalysts can selectively oxidizing NO to NO_2 rather than oxidizing SO_2 to SO_3, thereby causing the decrease of sulfate species. Our work provides a novel idea for the design of SCR catalysts with high activity and SO_2 resistance.

1. Introduction

Selective catalytic reduction of NO_x by NH_3 (NH_3-SCR) is considered to be the most widely used technology for NO_x abatement from stationary and mobile sources [1–3]. The V_2O_5–WO_3/TiO_2 catalyst has been used in industry for many years as a commercial NH_3-SCR catalyst. However, their high operating temperature window (300–400 °C) requires the SCR units to be located in front of the electrostatic precipitators and desulfurization units, which causes some problems: abrasion of the catalyst by dust particles, the deposition of ammonium sulfate causing blockage of downstream pipelines [1,4,5]. Therefore, it is highly desirable to develop the low-temperature (< 200 °C) vanadium-free catalysts to install the SCR units in the last unit of the reaction. Currently, most studies are devoted to the development of transition metal oxide catalysts as a replacement for toxic V-based oxide catalysts. Among these, manganese oxide (MnO_x) catalysts are considered desirable candidates for NH_3-SCR due to their outstanding redox properties and variable valence [6,7]. However, the limited operating temperature window, poor SO_2 resistance, and poor NH_3-SCR activity at high space velocity for pure MnO_x restrict their further application [5,8,9].

In recent years, many researchers have reported improving the NH_3-SCR activity and SO_2 tolerance of the MnO_x catalysts by introducing a second metal to tune the electronic structure of the manganese oxide [4,10,11]. However, most of the catalysts lack stable catalytic activity in an SO_2 atmosphere. This is because a small amount of SO_2 can be easily converted into SO_3 by oxidized metal sites [1]. The formation of SO_3 will sulfate active components, leading to loss of activity; meanwhile, SO_3 can react directly with NH_3 and H_2O to generate ammonium sulfate, which possesses a higher decomposition temperature than the reaction temperature of NH_3-SCR [12–14]. Therefore, it will occupy the active sites and block the pores of the catalysts. Effective inhibition of SO_2 oxidation to SO_3 is the key to improving SO_2 tolerance. The SO_2 oxidation can be effectively weakened by increasing electron-donating promoters to decline the oxidability of active sites and inhibiting the electron transfer from SO_2 to high valence Mn [1,10]. Sun et al. revealed that the electron transfer from SO_2 to Mn^{4+} can be effectively inhibited through the electron transfer from Sm^{2+} to Mn^{4+}, thereby inhibiting the generation of SO_3 and sulfate species [11]. Liu et al. revealed that the transfer of electrons from graphite carbon to Mn^{3+} in Mn_3O_4 can inhibit SO_2 oxidation to SO_3, which improves the SO_2 resistance of Mn_3O_4 [4]. Li et al. found that the transfer of electrons from SO_2 to Mn species is inhibited by doping V into the $MnCoO_x$ catalyst, thereby delaying SO_2 poisoning of the catalyst [10]. However, the robust catalytic performance of MnO_x catalysts is mainly attributed to their strong oxidation ability, which can promote the oxidation of NO to NO_2, thereby

---

triggering the "fast" SCR reaction [4,15]. Therefore, it is a key step to effectively tune the oxidability of MnO_x catalysts to selectively oxidize NO rather than SO_2.

Among many manganese oxides, the relatively low average valence state of the Mn element in Mn_3O_4 is conducive to attenuation of SO_2 oxidation, and the unique spinel structure of Mn_3O_4 with rich oxygen vacancies is beneficial to NO oxidation. Further modification is expected to simultaneously improve NH_3-SCR activity and SO_2 tolerance. At present, researchers are mainly focusing on the second metal modification, and the introduction of other heteroatoms such as (N, F, S, P) is rarely reported. Among many heteroatoms, F has the highest electronegativity and is considered to be a promising donor dopant for metal oxides [16–18]. In addition, F has a similar ionic radius to O ion, which gives F the ability to partially replace lattice oxygen, thus F doping will change the electronic structure or phase structure of metal oxides, which has a great impact on their redox kinetics [18,19]. The partial replacement of O by F in Mn_3O_4 will produce extra negative charges because F is monovalent [20]. The combination of negative charge and Mn^{3+} can effectively inhibit the transfer of electrons from SO_2 to Mn^{3+}, thus reducing SO_2 oxidation to SO_3. In addition, the surface Mn-O lattice distortion caused by F replacing O is easy to generate oxygen vacancies, which is conducive to NO oxidation. Therefore, a suitable F modification is expected to achieve a simultaneous improvement in NH_3-SCR and SO_2 resistance. However, there is no research on heteroatom F-doped Mn_3O_4 used in the low-temperature NH_3-SCR reaction.

Currently, metal-organic frameworks (MOFs) are widely used as precursors for the synthesis of metal oxides [21–23]. The metal oxides derived from MOFs not only inherit the advantages of MOFs such as large specific surface area, porosity and morphology but also can improve the dispersion of active components by the coordination network structure. Moreover, the active sites can also be accurately regulated by the coordination states of MOFs. Herein, we selected Mn-MOF-74 as the precursor, NH_4F as the fluorine source, and NH_4F was added during the hydrothermal synthesis of Mn-MOF-74 to make F^- uniformly dispersed in the cage of Mn-MOF-74. We further obtained F-doped Mn_3O_4 spinel catalysts by pyrolysis and oxidation of F-Mn-MOF-74. The NH_3-SCR performance of the F-Mn_3O_4-x catalysts was carried out under very severe conditions. Among them, F-Mn_3O_4-3 % exhibited excellent catalytic performance and NO conversion of more than 90 % from 150 °C to 310 °C under an ultra-high gas hourly space velocity (GHSV) of 400,000 h^{-1}. The SO_2 resistance was also significantly improved compared to pure Mn_3O_4. Therefore, through a variety of characterizations, we revealed the role of F on the structure and physicochemical properties of the Mn_3O_4 spinel catalyst. In addition, the NH_3-SCR reaction mechanism and the SO_2 resistance mechanism were also elucidated.

2. Experimental

2.1. Catalyst preparation

2.1.1. Preparation of F-Mn-MOF-74

The Mn-MOF-74 was prepared through a hydrothermal method according to our previous report [24]. And the F-Mn-MOF-74 was obtained by adding NH_4F in the preparation process of Mn-MOF-74. Further preparation details are given in the Supporting Information (SI).

2.1.2. Preparation of F-Mn_3O_4-x nanoparticles

The obtained F-Mn-MOF-74 was moved to a tube furnace and the temperature was raised to 600 °C at a rate of 2 °C/min in a stream of N_2 and thermally treated for 180 min. After cooling the furnace, the N_2 was shut off and the tube furnace inlet was opened for slow oxidation for 1 h. The samples were then moved to a muffle furnace and annealed at 350 °C for 240 min at a rate of 2 °C/min to obtain F-Mn_3O_4-x nanoparticles. All the catalysts involved in the NH_3-SCR reaction were pressed and crushed and the 40–60 mesh catalysts were sieved.

2.2. Structural characterization and catalytic activity test

The associated characterization techniques and application methods involved in the catalyst characterization process and the conditions for assessing catalyst activity are detailed in SI.

2.3. Theoretical calculations

Density function theory (DFT) calculations were obtained using the Vienna ab-initio simulation package (VASP) [25]. Details of the definition and calculation are given in the SI.

3. Results and discussion

3.1. Textural characteristic

Fig. 1a exhibits the synthesis process of the F-doped Mn_3O_4 spinel catalysts using Mn-MOF-74 as the precursors. Since the ionic radius of F is much smaller than the cage of Mn-MOF-74, F ions can easily enter into the cage of Mn-MOF-74 by introducing F ions during the hydrothermal synthesis of Mn-MOF-74. The X-ray diffraction (XRD) patterns (Fig. 1b) show that the peak position of the F-doped Mn-MOF-74 is the same as that of the simulated MOF-74. The F-doped Mn-MOF-74 precursors were pyrolyzed in an N_2 atmosphere at 600 °C. The XRD patterns of the obtained products (Fig. S1) show that all the pyrolyzed F-doped Mn-MOF-74 exhibit characteristic peaks of MnO (PDF No. 01-78-0424). Thermogravimetric analysis (TGA) (Fig. S2) shows that the amorphous carbon species formed during the pyrolysis process are completely decomposed at 350 °C in the air atmosphere. Therefore, the desired samples of F-doped Mn_3O_4 catalysts were achieved by oxidizing the pyrolyzed F-doped Mn-MOF-74 at 350 °C and were designated as F-Mn_3O_4-x (x represents the F/Mn molar ratio in the reactant). The XRD results (Fig. 1c, Fig. S3) exhibit that all the characteristic peaks of F-Mn_3O_4-x are consistent with the Mn_3O_4 (PDF No. 01-075-1560) and with an *I41/amd* space group, except for the F-Mn_3O_4-15 % catalyst, which appears the MnF_2 character peak. To ensure a high-purity phase of the F-doped Mn_3O_4 spinel structure, F-Mn_3O_4-3 % and Fe-Mn_3O_4-10 % catalysts are selected for further study. In addition, with increasing F content, the positions (Fig. S4) of the characteristic peaks (2θ = 28.7, 32.4, 35.9) of F-Mn_3O_4-x are shifted to a high degree, indicating that F with a smaller ionic radius has been integrated into the lattice of Mn_3O_4 by partially replacing the O position [5].

The morphology of F-Mn_3O_4-x spinel nanoparticles was analyzed using transmission electron microscopy (TEM) techniques. As shown in Fig. 1d and Fig. 1f, Mn_3O_4 and F-Mn_3O_4-3 % exhibit hexagonal rod structures stacked by uniform nanoparticles, and the morphology of the Mn_3O_4 catalyst is not affected by F-doping. The HRTEM image of Mn_3O_4 is shown in Fig. 1e, the Mn_3O_4 exhibits obvious lattice fringes with the lattice spacings of 0.275, 0.247, 0.228, 0.203, and 0.196 nm, corresponding to the (103), (211), (004), (220), and (213) crystal planes of Mn_3O_4. For the F-Mn_3O_4-3 % catalyst (Fig. 1g), the lattice spacings of the (211) and (004) crystal planes are slightly smaller than those of Mn_3O_4 (0.246 < 0.247, 0.226 < 0.228), indicating that F with a smaller ionic radius is doped in the lattice of Mn_3O_4 by replacing the position of O [13]. The elemental mapping images (Fig. 1h-l) show a high dispersion of Mn, O, and F in F-Mn_3O_4-3 %, suggesting uniform incorporation of F into the bulk phase of Mn_3O_4 [13]. At the same time, the TEM image of the F-Mn_3O_4-10 % catalyst is illustrated in Fig. S5a-b. Compared to the F-Mn_3O_4-3 % catalyst, the F-Mn_3O_4-10 % still exhibits a hexagonal rod structure despite the increase in F doping amount, indicating that the morphology of the catalysts is not affected by the increase of F doping amount. The elemental mapping images (Fig. S5c-g) of F-Mn_3O_4-10 % show that Mn, O and F are still highly dispersed.

The structure and porosity of the catalysts were investigated (Fig. S6 and Table S1) using the N_2 adsorption-desorption technique. After the introduction of F, the Brunauer-Emmett-Teller (BET) specific surface
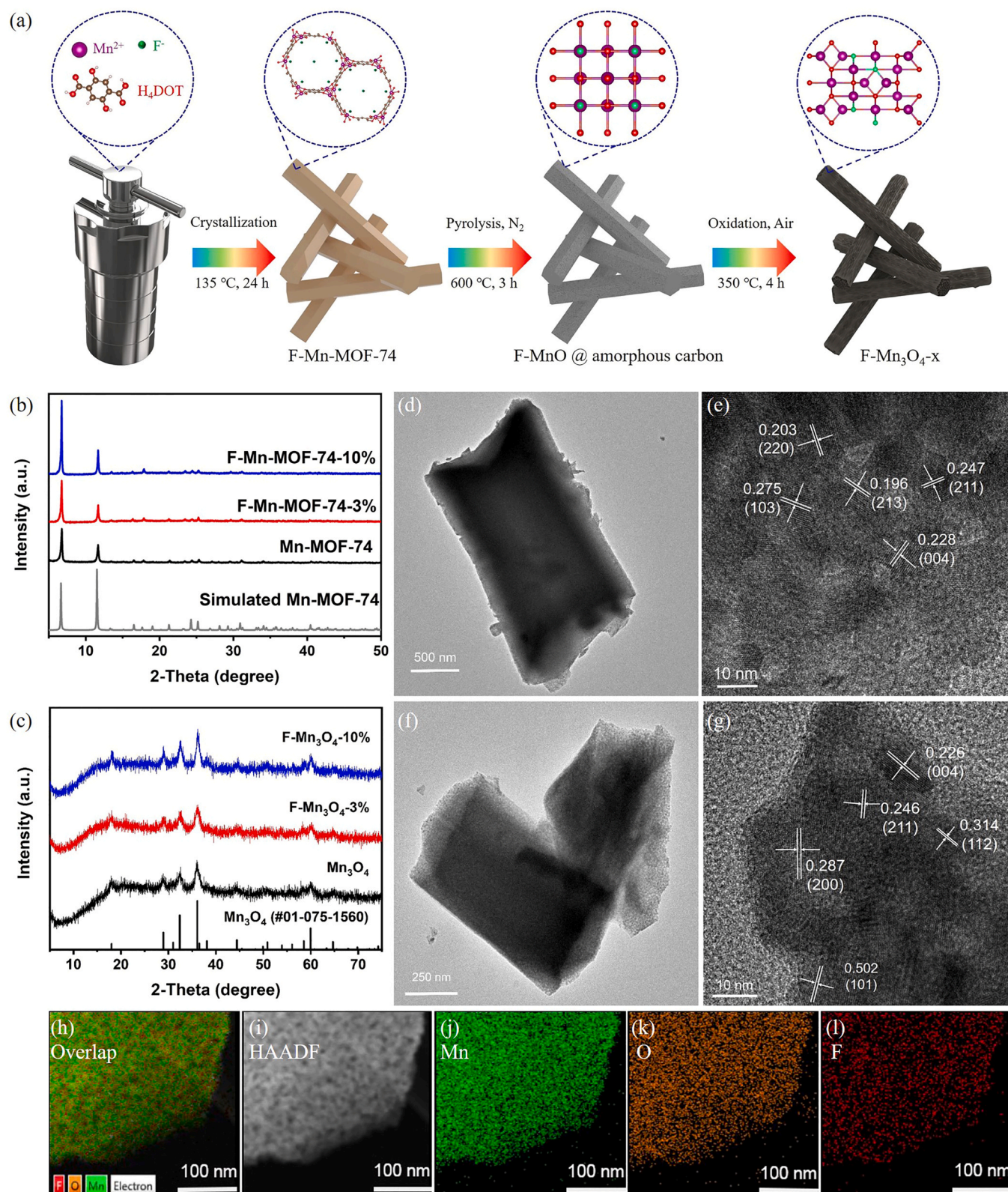
Fig. 1. (a) The preparation process of the F-Mn$_3$O$_4$-x catalysts; XRD patterns of F-doped Mn-MOF-74 (b) and F-Mn$_3$O$_4$-x nanoparticles (c); TEM and HRTEM images of Mn$_3$O$_4$ (d-e) and F-Mn$_3$O$_4$-3 % (f-g); (h-l) elemental mapping of F-Mn$_3$O$_4$-3 %.

area of the F-Mn$_3$O$_4$-3 % (89.2 m$^2 \cdot$g^{-1}) increased significantly compared to Mn$_3$O$_4$ (53.5 m$^2 \cdot$g^{-1}). However, with a further increase in F content, the specific surface area of the F-Mn$_3$O$_4$-10 % (74.1 m$^2 \cdot$g^{-1}) decreased. Among them, F-Mn$_3$O$_4$-3 % has the largest specific surface area, which is advantageous for F-Mn$_3$O$_4$-3 % to expose more active sites and adsorb

more reactant species.

3.2. Surface chemical properties

The chemical state and relative concentration of the elements near

the catalyst surface were analyzed by the X-ray photoelectron spectroscopy (XPS) technique. The average oxidation state (AOS) of the Mn element is confirmed through the Mn 3 s spectra (Fig. 2a). The AOS is usually calculated using the formula AOS = $8.956 - 1.126 \triangle E_s$, where $\triangle E_s$ represents the distance between the two peaks in the Mn 3 s [7,26, 27]. The order of the AOS is Mn_3O_4 (3.04) > F-Mn_3O_4-3 % (2.93) > F-Mn_3O_4-10 % (2.76), indicating that the AOS gradually decreases as the F doping content increases. The Mn 2p XPS spectra (Fig. 2b) show that two peaks allocated to Mn $2p_{1/2}$ and Mn $2p_{3/2}$ orbitals can be observed. The binding energy shifts to lower energies with increasing F content, indicating that the Mn^{3+} has obtained electrons. The detailed contents of Mn^{3+} (642.2 and 653.4 eV) and Mn^{2+} (640.9 and 652.1 eV) can be determined by fitting Mn $2p_{1/2}$ and Mn $2p_{3/2}$ [28,29]. As shown in Table S2, the Mn^{3+}/Mn^{2+} molar ratio in Mn_3O_4 is 1.86, which is significantly higher than F-Mn_3O_4-3 % (1.22) and F-Mn_3O_4-10 % (0.99).

The O 1 s XPS spectra (Fig. 2c) can be divided into three regions, corresponding to lattice oxygen (O_L, 529.8 eV), oxygen vacancies (O_V, 531.0 eV) and chemisorbed oxygen species (O_C, 532.7 eV), respectively [30,31]. The low-temperature NH_3-SCR activity of MnO_x catalysts is closely related to their NO oxidation ability [5,24]. NO oxidation requires the participation of surface adsorbed oxygen, which is mainly derived from the activation of molecular oxygen [4,5,8]. O_V plays a key

role in the process of molecular oxygen activation, thereby the formation of O_V is crucial in the process of NO oxidation [4,5]. Compared to pure Mn_3O_4, the O_V content increases with increasing F content, indicating that F doping causes lattice distortion and produces more surface defects. In addition, F 1 s XPS peaks (Fig. S7) are detected in both F-Mn_3O_4-3 % and F-Mn_3O_4-10 % catalysts, which also indicates that F is successfully doped.

The bulk defects of the catalysts were further investigated by the electron paramagnetic resonance (EPR) technique as shown in Fig. 2d. Each catalyst exhibits a symmetric EPR signal at g = 2.003, which represents the unpaired electrons on the oxygen vacancies of the catalysts, and the signal intensity corresponds to the oxygen vacancy content [13,32]. Among them, Mn_3O_4 exhibits the weakest EPR signal, corresponding to the lowest number of oxygen vacancies. As the amount of F doping increases, the bulk oxygen vacancies content increases, which is consistent with the XPS results and indicates that F doping contributes to the formation of oxygen vacancies in Mn_3O_4. The presence of oxygen vacancies is advantageous for the promotion of NO oxidation and thus improving the NH_3-SCR activity [5,7].

X-ray absorption fine structure (XAFS) is an effective technique for determining the electronic structure and coordination environment of F-doped Mn_3O_4 catalysts. The X-ray absorption near edge structure
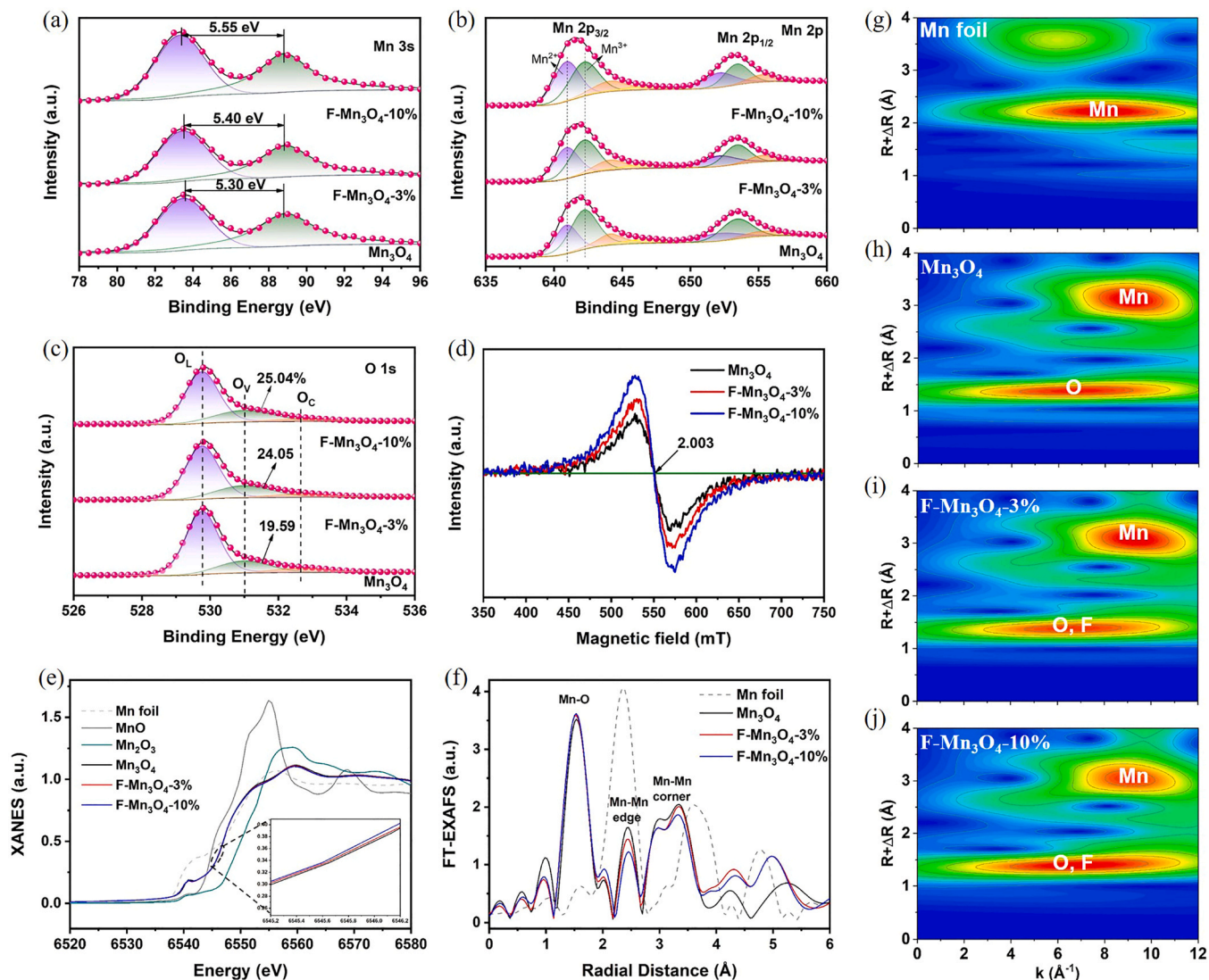

Fig. 2. (a) Mn 3 s, (b) Mn 2p and (c) O l s XPS spectra for the F-Mn_3O_4-x catalysts; (d) EPR spectra, (e) Mn K-edge XANES spectra and (f) FT EXAFS spectra for F-Mn_3O_4-x catalysts. WT plots at the Mn K-edge of (g) Mn foil, (h) Mn_3O_4, (i) F-Mn_3O_4-3 % and F-Mn_3O_4-10 %.

(XANES) spectra of the Mn K-edge (Fig. 2e) exhibit that the absorption edge of the F-Mn$_3$O$_4$-x catalyst is located between MnO and Mn$_2$O$_3$, which means that the Mn species valence is between + 2 and + 3. Compared to pure Mn$_3$O$_4$, the absorption edge of catalysts with increased F doping amount shifts towards the low energy direction, indicating that the average valence state of Mn reduces after F doping, which is consistent with XPS results. The Fourier-transformed k^3-weighted extended X-ray adsorption fine structure (EXAFS) spectra (Fig. 2f) of the F-Mn$_3$O$_4$-x catalyst show that there are mainly three regions. The first region is located at 1.6 Å and corresponds to the Mn-O distances, and the next region is located at about 2.4 and 3.2 Å can be attributed to the Mn-Mn distances in edge-shared octahedra and Mn-Mn in corner-shared tetrahedral [4,33]. The ratio of Mn-Mn bonding

strength at 2.4 and 3.2 Å decreases with increasing F content, indicating that part of the Mn^{3+} is reduced to Mn^{2+} by gaining electrons. The wavelet transforms (Fig. 2g-j) of F-Mn$_3$O$_4$-x exhibit that there are two maxima at (6.4 Å^{-1}, 1.4 Å) and (9.2 Å^{-1}, 3.1 Å), which coincides with the scattering of Mn-O (F) and Mn-Mn, respectively.

3.3. Redox properties and acidity

It is widely accepted that the appropriate redox properties are essential for improving the NH$_3$-SCR activity of the catalysts. The H$_2$-temperature programmed reduction (H$_2$-TPR) was used to evaluate the redox performance of the catalysts. The H$_2$ consumption of different oxygen species is summarized in Fig. 3a-b and Table S3. It can be seen
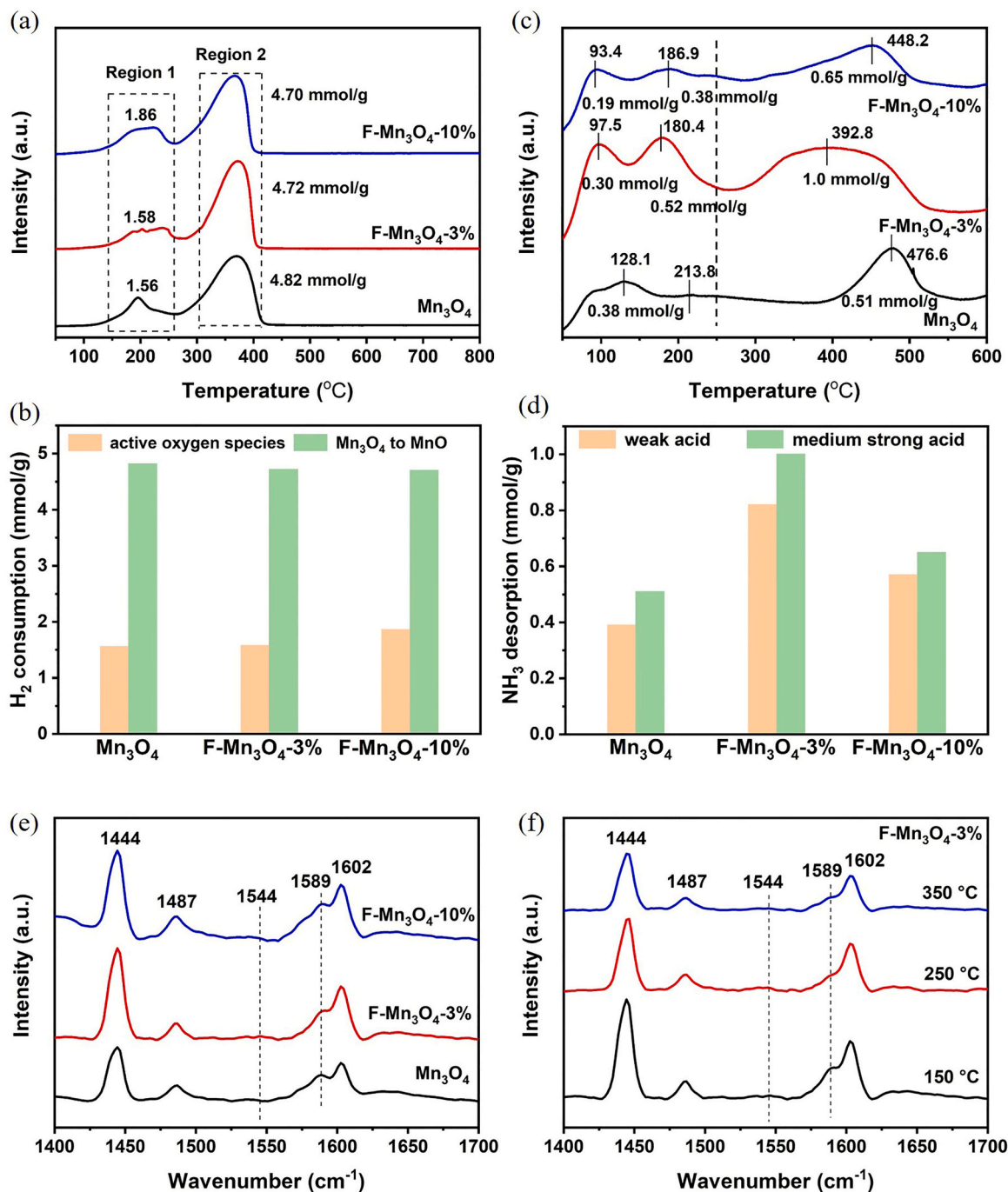

Fig. 3. (a) H$_2$-TPR profiles of F-Mn$_3$O$_4$-x catalysts and corresponding to H$_2$ consumption amount (b); (c) NH$_3$-TPD profiles of F-Mn$_3$O$_4$-x catalysts and corresponding to NH$_3$ desorption amount (d). Pyridine IR spectra of F-Mn$_3$O$_4$-x at 150 °C (e) and F-Mn$_3$O$_4$-3 % from 150° to 350°C (f).

that two reduction regions appeared for all catalysts. The first region is located at about 150–250 °C, which belongs to the reduction of highly active oxygen species adsorbed on the surface oxygen vacancies, the content of highly active oxygen species can indirectly reflect the number of oxygen vacancies [34,35]. The sequence of H_2 consumption is as follows: Mn_3O_4 (1.56) < F-Mn_3O_4-3 % (1.58) < F-Mn_3O_4-10 % (1.86), implying that the F-Mn_3O_4-10 % possesses the largest number of oxygen vacancies, which is the same as XPS and EPR results. The second region located at about 250–420 °C is due to the reduction of Mn_3O_4 to MnO [34]. The reduction temperature of region 2 is unchanged with the increase of F content, but the H_2 consumption decreases, which is due to the decrease of Mn^{3+} content in Mn_3O_4 after the introduction of F, corresponding to XPS and EXAFS results.

Apart from the redox properties, surface acidity is another key factor to increase the NH_3-SCR activity of the catalysts. The NH_3-temperature programmed desorption (NH_3-TPD) was used to investigate the surface acidity of the F-Mn_3O_4-x catalysts. The amount of NH_3 desorption was integrated based on the area of each peak and normalized and quantitatively evaluated as shown in Fig. 3c-d and Table S4. All catalysts can be divided into two regions. The first region located at 50–250 °C can be attributed to NH_3 adsorbed on weak acid sites and the second region (250–500 °C) is attributed to NH_3 adsorbed on medium-strong acid sites [36]. With the introduction of F into Mn_3O_4, the weak acid and medium-strong acids are significantly increased. In particular, the surface of F-Mn_3O_4-3 % has the largest number of acid sites. The increase of acid sites contributes to NH_3 species adsorption, which will boost the low-temperature NH_3-SCR reaction.

Due to NH_3-TPD cannot distinguish the types of acid sites well, the pyridine IR experiments were performed to further identify the types of acid sites. The pyridine adsorbed on F-Mn_3O_4-x catalysts at 150 °C and

on F-Mn_3O_4-3 % from 150° to 350°C is shown in Fig. 3e-f. The peaks at 1444 and 1602 cm^{-1} belong to the NH_3 adsorbed on Lewis acid sites, the peaks at 1544 and 1589 cm^{-1} correspond to NH_4^+ adsorbed on Brønsted acid sites, and the peak at 1487 cm^{-1} is assigned to the combination of Lewis acid and Brønsted acid sites [36–38]. F-Mn_3O_4-x catalysts are mainly dominated by Lewis acid sites. The order of acid strength is F-Mn_3O_4-3 % > F-Mn_3O_4-10 % > Mn_3O_4, indicating that F doping increases the content of acid sites of Mn_3O_4. With the increase in desorption temperature to 350 °C, the intensity of all peaks can still be above 50 %, which guarantees the subsequent NH_3-SCR reaction.

3.4. Activity evaluation

The NH_3-SCR performance of the F-Mn_3O_4-x catalysts is displayed in Fig. 4a and Fig. S8. The results show that the pure Mn_3O_4 exhibits relatively poor NH_3-SCR performance, the light-off temperature (T50, temperature at which NO conversion achieves 50 %) of NO is close to 155 °C, and the maximum NO conversion only reaches 82 % at 280 °C under the GHSV of 300,000 h^{-1}. Surprisingly, the NO conversion achieves a significant improvement after the introduction of F in Mn_3O_4. Among them, F-Mn_3O_4-3 % shows excellent NH_3-SCR activity, and the T50 value drops to 80 °C, which is 75 °C lower than that of Mn_3O_4. And the NO conversion is over 90 % in the range of 140–310 °C. Compared with Mn_3O_4, the N_2 selectivity (Fig. S9) is also significantly enhanced after the introduction of F. Moreover, the NO conversion of F-Mn_3O_4-3 % remains above 90 % during the stability test for 48 h at 140 °C (Fig. S10), representing excellent reaction stability. The XRD pattern (Fig. S11) reveals that the crystal structure of F-Mn_3O_4-3 % has barely changed after the stability test, demonstrating that F-Mn_3O_4-3 % has great structural stability. The GHSV is an important index in practical
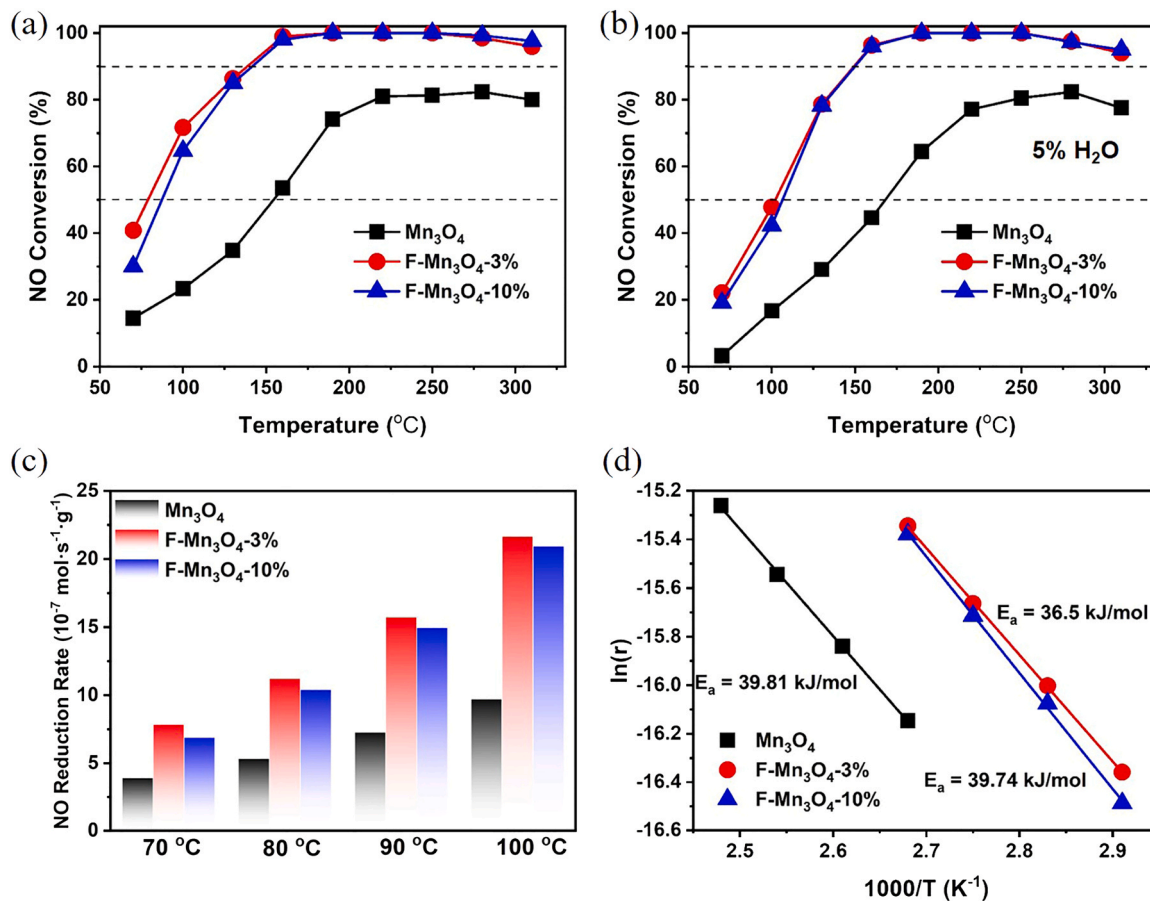

Fig. 4. (a) NH_3-SCR activity and (b) NH_3-SCR activity with 5% water vapor of F-Mn_3O_4-x catalysts under the GHSV of 300,000 h^{-1}; (c) NO reduction reaction rate and (d) Arrhenius plots of F-Mn_3O_4-x catalysts under the GHSV of 2,000,000 h^{-1}.

applications. The NH₃-SCR performance of the F-Mn₃O₄-3 % at a GHSV of 300,000–400,000 h⁻¹ is shown in Fig. S12a-b. Even at an ultra-high GHSV of 400,000 h⁻¹, the F-Mn₃O₄-3 % catalyst can still achieve a T50 at 90 °C and exceed 90 % NO conversion at 150 °C, which is competitive with many MnOₓ catalysts (Table S5).

In practical industrial applications, water vapor is an inevitable factor in the deterioration of catalyst activity. The NH₃-SCR performance (Fig. 4b) of the F-Mn₃O₄-x catalysts with 5 % steam exhibits that the NO conversion of the F-Mn₃O₄-x significantly decreases below 130 °C, which is attributed to the competitive adsorption between H₂O and NH₃/NO [8]. However, the NO conversion is almost unaffected by water vapor when the reaction temperature exceeds 130 °C.

The intrinsic activity of the catalyst can be evaluated through the reaction rate (r), and the apparent activation energy (E_a) using reaction kinetics experiments when the NO conversion is less than 20 %. As shown in Fig. 4c, the NO reduction reaction rate of pure Mn₃O₄ is relatively inferior, indicating a lower catalytic efficiency. With the increase of F content, the NO reduction reaction rate shows a volcanic trend, and the F-Mn₃O₄-3 % catalyst has the highest reaction rate, corresponding to a higher intrinsic activity. The E_a is calculated by the Arrhenius equation (Fig. 4d). However, a similar E_a was displayed for F-Mn₃O₄-x catalysts, which might be attributed to F having a little effect on the active catalytic sites of the Mn₃O₄ catalyst for the NH₃-SCR [39]. In addition, the specific surface area is an important influencing factor for improving catalytic activity and therefore NO reduction reaction rate normalized to the specific surface area is also carried out (Fig. S13). It can be seen that the NO reduction reaction rate normalized to the specific surface area is still significantly higher for F-doped Mn₃O₄ catalysts than for pure Mn₃O₄, indicating that F-doped Mn₃O₄ catalysts possess a higher catalytic efficiency.

It has been acknowledged that the "fast" SCR reaction plays a dominant role in low-temperature SCR reactions. In the "fast" SCR reaction, the NO/NO₂ molar ratio should be equal to 1, making the NO oxidation crucial [8,40]. The NO oxidation performance of the F-Mn₃O₄-x catalysts (Fig. S14) shows that pure Mn₃O₄ possesses inferior NO oxidation activity. With the incorporation of F into Mn₃O₄, the NO oxidation activity is significantly improved. Among them, F-Mn₃O₄-3 % has the best NO oxidation performance, which corresponds to its efficient NH₃-SCR activity.

Although the SO₂ content in the flue gas is significantly reduced after the desulfurization device, the residual SO₂ also reduces the activity of the catalyst. Therefore, the SO₂ resistance of the catalysts in the SCR process must be considered. The H₂O + SO₂ tolerance (Fig. 5a) of the F-Mn₃O₄-x catalysts shows that the NO conversion of all catalysts decreases slightly upon 5 % H₂O introduction into the reaction system. However, the NO conversion of Mn₃O₄ drops rapidly from ∼ 96 to ∼ 39 % with the introduction of SO₂ at 240 min. In contrast, the SO₂ tolerance is significantly enhanced after the incorporation of F into Mn₃O₄. Among them, the F-Mn₃O₄-3 % catalyst exhibits better SO₂ tolerance than the F-Mn₃O₄-10 % catalyst. And the NH₃-SCR activity of the F-Mn₃O₄-x catalysts has a certain improvement after the removal of SO₂ and H₂O, but it cannot be restored to the initial state, signifying that the SO₂ deactivation of the catalysts is irreversible. The S 2p XPS analysis of the F-Mn₃O₄-x after the reaction is shown in Fig. 5b. The intensity of sulfur species on the surface of the F-Mn₃O₄-3% is significantly lower than that of Mn₃O₄ and F-Mn₃O₄-10 %, indicating that the lowest sulfur species content is on the surface of F-Mn₃O₄-3 %. The S 2p can be divided into three regions, the first region located at 168.2 eV can be assigned to SO_3^{2-}, and the next region located at 169.2 and 169.7 eV belongs to SO_4^{2-} [4,13]. The SO_4^{2-} is the main sulfur species on the catalyst surface.
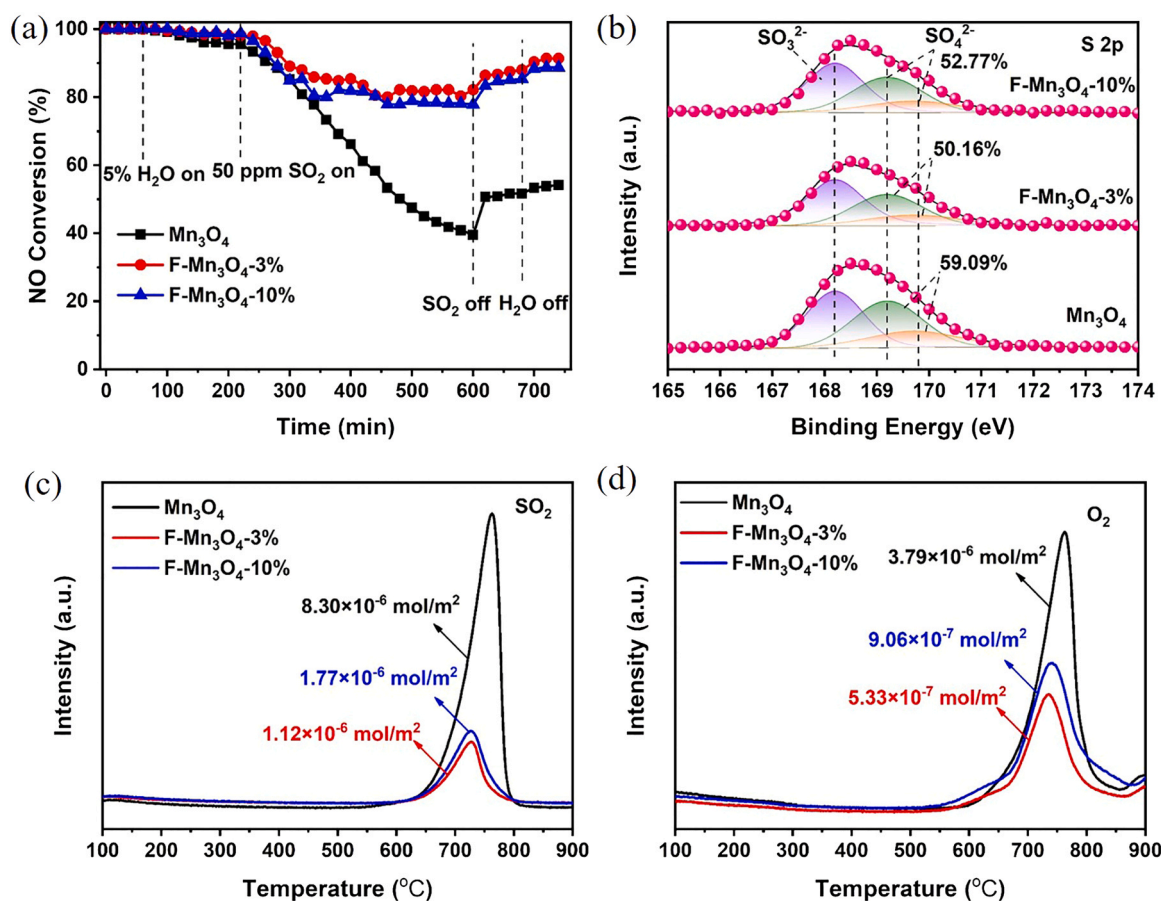

Fig. 5. (a) H₂O + SO₂ resistance tests of F-Mn₃O₄-x catalysts (160 °C, 60, 000 h⁻¹); (b) S 2p XPS spectra of F-Mn₃O₄-x catalysts after H₂O + SO₂ resistance tests; MS signal of SO₂ (c) and (d) O₂ over F-Mn₃O₄-x.

Additionally, the proportion of SO_4^{2-} on the catalyst surface is Mn_3O_4 (59.09 %) > F-Mn_3O_4-10 % (52.77 %) > F-Mn_3O_4-3% (50.16 %), indicating that F-Mn_3O_4-3 % has the weakest SO_2 oxidation ability. The Mn 2p XPS spectra (Fig. S15) of F-Mn_3O_4-x after the SO_2 resistance test showed that the ratio of Mn^{3+} on the Mn_3O_4 surface is 35.12 %, which is significantly lower than F-Mn_3O_4-3 % (41.12 %) and F-Mn_3O_4-10 % (38.82 %), indicating that the electron transfers from SO_2 to Mn^{3+} after F doping into Mn_3O_4 can be effectively inhibited.

The He-temperature programmed desorption (He-TPD) technique was used for further quantitative analysis of the sulfur species on the F-Mn_3O_4-x catalysts, and the decomposed gases were detected online through mass spectroscopy (MS). The He-TPD spectra (Fig. S16) reveal that there are two desorption peaks on all catalysts. The first desorption peak at ~ 335 °C is due to the decomposition of NH_4HSO_4 [4,12,41]. At the same time, the MS signals of NH_3 and H_2O are detected at peak 1 (Fig. S17a-b). And the MS signals (Fig. 5c-d) of SO_2 and O_2 are detected at peak 2, the SO_2/O_2 molar ratio is close to 2, which matches the decomposition products of SO_3. The high decomposition temperature of 730 ~ 765 °C is consistent with that of $MnSO_4$, so it can be concluded that peak 2 belongs to the decomposition of $MnSO_4$ [12,41,42]. In addition, He-TPD spectra show that the intensity of sulfur species on the surface of F-Mn_3O_4-3 % and F-Mn_3O_4-10 % is much lower than that of Mn_3O_4. Therefore, the negative charge generated after F replaces O combined with Mn^{3+} can effectively inhibit the transfer of electrons from SO_2 to Mn^{3+}, thereby reducing the generation of SO_3 and causing the decrease of sulfate species. However, the TCD signal intensities of F-Mn_3O_4-10 % at peaks 1 and 2 exceed those of F-Mn_3O_4-3 %, indicating that the surface of the F-Mn_3O_4-10 % catalyst contains more sulfate species, corresponding to its relatively weak SO_2 resistance. The decrease in the number of acid sites is probably the reason to explain the decline of SO_2 tolerance of the F-Mn_3O_4-10 % catalyst compared to the F-Mn_3O_4-3 % catalyst. Since SO_2 adsorption is considered to be the first step in the SO_2 deactivation of MnO_x catalysts [1]. Increasing the surface

acidity of the catalyst can effectively inhibit SO_2 adsorption and oxidation, thus improving the SO_2 resistance of the catalysts [1,35]. In conclusion, the enhancement of SO_2 tolerance of F-doped Mn_3O_4 is the synergistic effect of increasing the number of acid sites and inhibiting the electron transfer from SO_2 to Mn^{3+}.

3.5. Density functional theory calculation

The influence of F-substituted O on the electron distribution of the Mn octahedral site was analyzed using charge density difference plots. Due to more electrons in the outer layers of F, the Mn-F interaction is weakened and more electrons are present on the surface of the Mn octahedral site (Fig. 6a), which can be confirmed by the electron localization function map (Fig. S18). Furthermore, Bader charge analysis quantifies the surface electronic state, the Bader charge value of Mn sites increases from 11.228 (11.227) to 11.264 (11.299) after F replacement (Fig. S19 and Table S6), signifying that more electrons are transferred to Mn^{3+}.

Additionally, the electronic effects between SO_2 and Mn_3O_4 are further investigated. Due to more electrons on the surface of Mn after F replaces O, the interaction of Mn-S is greatly weakened when the SO_2 adsorbed on the Mn_3O_4 (Fig. 6b-c, Fig. S20), indicating that the SO_2 adsorption and oxidation are more difficult on the Mn_3O_4 surface. This can be verified by the calculated SO_2 adsorption energy (Mn_3O_4 −0.26 eV, F-Mn_3O_4 −0.15 eV) and SO_3 generation energy (Mn_3O_4 −3.06 eV, F-Mn_3O_4 −2.63 eV) (Fig. 6d), which corresponds to the practical experimental results. The bader charge analysis (Fig. S21 Table S7) further reveals the effect of SO_2 adsorption on charge distribution. The valence electron number at the Mn octahedral site increases after SO_2 is adsorbed on Mn_3O_4, demonstrating that SO_2 transfers electrons to Mn^{3+}. The valence electron number at the Mn octahedral site increases by only 0.197 after the introduction of F, which is less than that of Mn_3O_4 (0.613), indicating that the electron conduction between
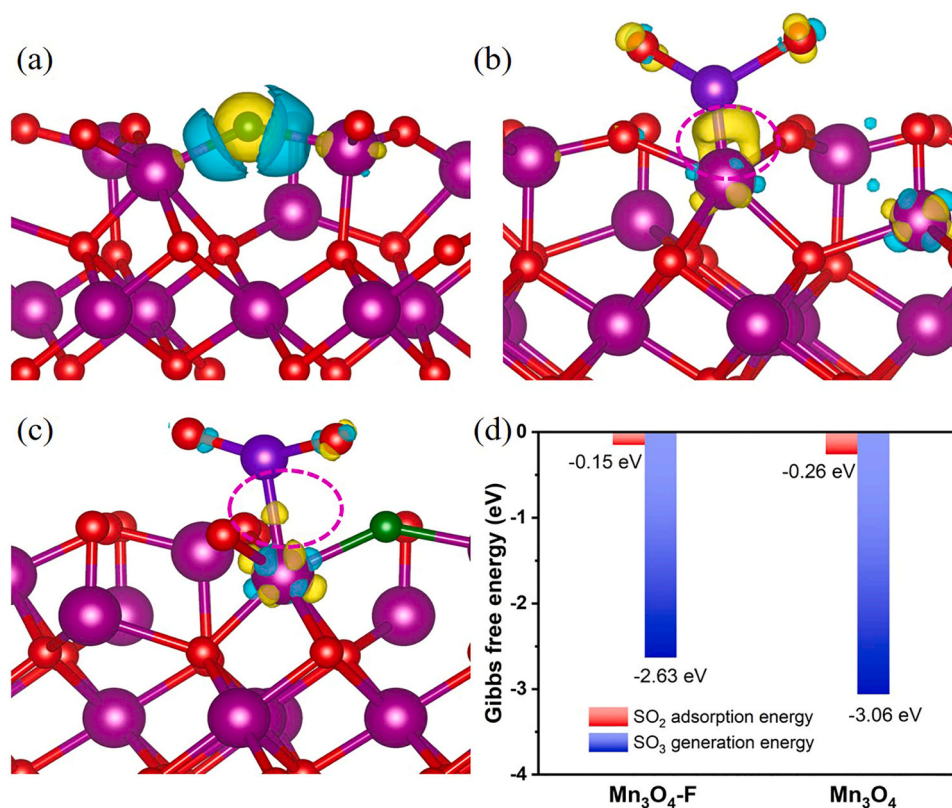

Fig. 6. Charge density difference plot for F doped Mn_3O_4 (a), SO_2 adsorbed on Mn octahedral site for Mn_3O_4 (b) and F-Mn_3O_4 (c), SO_2 adsorption and SO_3 generation energy over Mn_3O_4 and F-Mn_3O_4 (d).

SO_2 and Mn^{3+} can be effectively inhibited after F doping. In addition, the valence electron number of SO_2 after adsorption on the catalyst surface is 17.662 and 17.767 for Mn_3O_4 and F-doped Mn_3O_4, which also indicates that SO_2 transfers fewer electrons after adsorption on F-doped Mn_3O_4, thus powerfully inhibiting the oxidation of SO_2 to SO_3.

3.6. In situ drifts and mechanism

To better reveal the difference of F doping on Mn_3O_4 in the NH_3-SCR, the *in situ* DRIFTS technique is applied to investigate the adsorption behavior of reaction species and the transient reaction process on the Mn_3O_4 and F-Mn_3O_4-3 % catalyst. Fig. 7a-b exhibits the *in situ* DRIFTS spectra of NH_3 species adsorbed on Mn_3O_4 and F-Mn_3O_4-3 % surfaces at 100 °C. For Mn_3O_4, introducing NH_3/N_2 into the reaction for 30 min produces two peaks at 1203 and 1603 cm^{-1}, which are assigned to NH_3 adsorbed on Lewis acid sites [37,43]. A faint peak at 1433 cm^{-1} is ascribed to the adsorption of NH_4^+ on the Brønsted acid sites, and the characteristic peak at 1563 cm^{-1} is assigned to the NH_2 species [36,44]. However, for F-Mn_3O_4-3 %, the peak intensities at the Lewis acid sites (1186, 1603 cm^{-1}) and the Brønsted acid sites (1435 cm^{-1}) are much stronger than those of the Mn_3O_4 catalyst, especially the NH_4^+ adsorbed on the Brønsted acid site, which is essential for promoting the NH_3-SCR reaction. The above results reveal that F-Mn_3O_4-3 % has more acid sites, which is supported by NH_3-TPD.

The *in situ* DRIFTS spectra of $NO + O_2$ co-adsorption on the Mn_3O_4 and F-Mn_3O_4-3 % catalysts at 100 °C are performed (Fig. 7c-d). Several distinct peaks appear on the Mn_3O_4 upon introduction of $NO + O_2 / N_2$ into the *in situ* cell for 30 min, which belongs to monodentate nitrate (1272, 1528 cm^{-1}), bidentate nitrates (1548 cm^{-1}) and adsorbed NO_2

(1625 cm^{-1}), respectively [28,41,42,45]. Compared to Mn_3O_4, a new peak is observed at 1564 cm^{-1} for the F-Mn_3O_4-3 % catalyst, which also belongs to bidentate nitrates [41,42]. Obviously, the peak intensity of the surface nitrates and adsorbed NO_2 on the F-Mn_3O_4-3 % catalyst is much higher than that of Mn_3O_4, indicating that the adsorption amount of NO_x species increases after F is doped into the Mn_3O_4 catalyst, which is consistent with the above NO oxidation experiments.

To accurately reveal the changes of reactants over the catalysts under reaction conditions, the experiment between $NO + O_2$ and pre-adsorbed NH_3 species on the Mn_3O_4 and F-Mn_3O_4-3 % catalysts at 100 °C are recorded. As shown in Fig. 8a-b, the sample is first pretreated in an NH_3/N_2 atmosphere for 30 min, then purged with N_2, and then $NO + O_2$ is added. For Mn_3O_4, the peaks of NH_3 adsorbed on the Lewis acid sites at 1203 and 1606 cm^{-1} decrease slowly and vanish completely after 20 min of exposure to $NO + O_2$, and the peak of NH_4^+ adsorbed on Brønsted acid site at 1433 cm^{-1} disappears completely at 5 min. Meanwhile, the peaks of monodentate nitrates (1250, 1275, and 1517 cm^{-1}) and adsorbed NO_2 (1625 cm^{-1}) appear successively at 10 min. Furthermore, a new peak at 1443 cm^{-1} is observed, which belongs to the intermediate (M-O-NO_2-NH_3) generated by the interaction between adsorbed NO_x and NH_3, and it is decomposed into N_2 and H_2O above 180 °C [35]. However, the *in situ* DRIFTS result of the F-Mn_3O_4-3 % catalyst is significantly different. It can be seen (Fig. 8b) that the reaction rate between NO_x species and pre-adsorbed NH_3 species is significantly faster compared to Mn_3O_4, and the NH_3 coordinated with Lewis acid site completely disappears at 10 min. F-Mn_3O_4-3 % has the largest amount of NH_3 adsorption species, while the reaction rate is significantly faster than Mn_3O_4, indicating that the NH_3-SCR reaction rate can be improved after F doping of Mn_3O_4. At the same time,
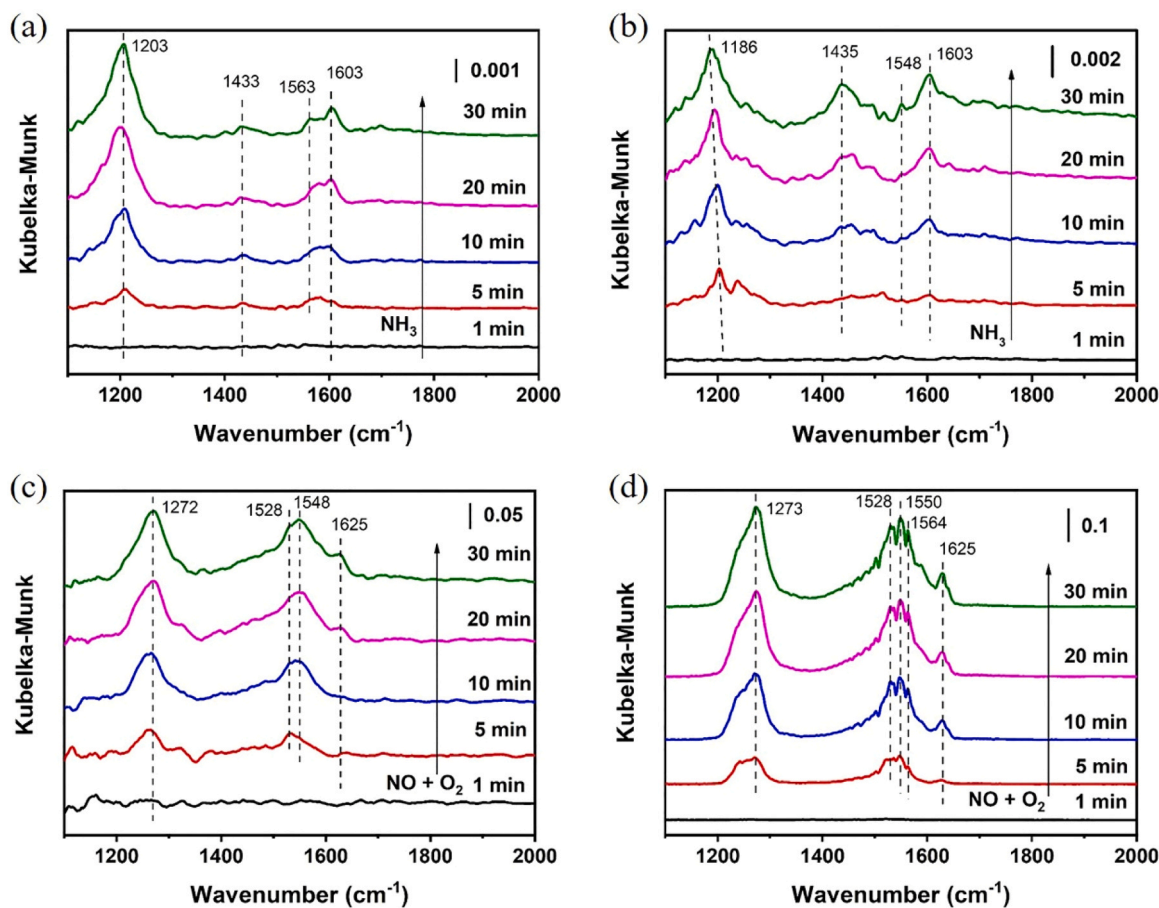

Fig. 7. *In situ* DRIFTS spectra of NH_3 adsorption over Mn_3O_4 (a) and (b) F-Mn_3O_4-3 % at 100 °C and $NO + O_2$ co-adsorption over Mn_3O_4 (c) and (d) F-Mn_3O_4-3 % at 100 °C.
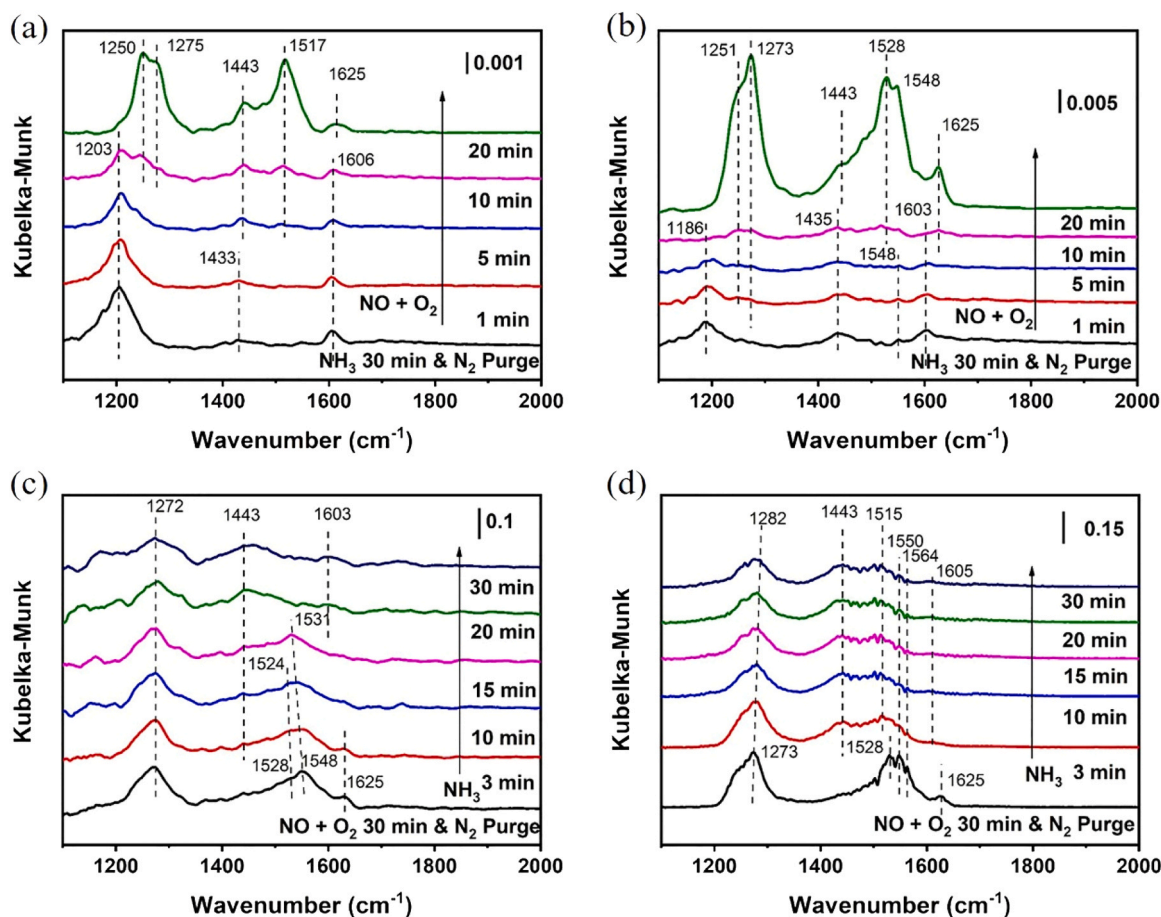
Fig. 8. *In situ* DRIFTS spectra of the reaction between NO + O$_2$ and pre-adsorbed NH$_3$ at 100 °C over Mn$_3$O$_4$ (a) and F-Mn$_3$O$_4$-3 % (b) and NH$_3$ reacting with pre-adsorbed NO + O$_2$ over Mn$_3$O$_4$ (c) and F-Mn$_3$O$_4$-3 % (d).
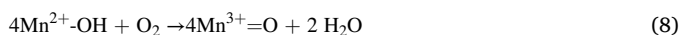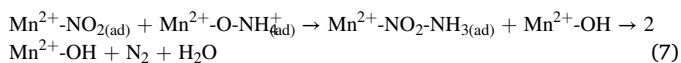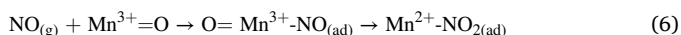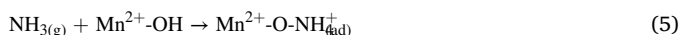
characteristic peaks ascribed to monodentate nitrates (1251, 1273, 1528 cm^{-1}), bidentate nitrates (1548 cm^{-1}) and adsorbed NO$_2$ (1625 cm^{-1}) are observed. In addition, the intermediate (M-O-NO$_2$-NH$_3$) is also found at 1443 cm^{-1}. Since the decomposition temperature of M-O-NO$_2$-NH$_3$ is above 180 °C, there may be another intermediate below 180 °C [35]. The appearance of NH$_2$ species in the process of NH$_3$ adsorption and its disappearance after the introduction of NO + O$_2$ indicates that NH$_2$NO is an important intermediate below 180 °C. From the above analysis, the NH$_3$-SCR reaction follows the Eley-Rideal (E-R) mechanism, in which coordinated NH$_3$ is dehydrogenated by the adjacent atom to form NH$_2$ species, and NH$_2$ can react with gaseous NO to generate the intermediate of NH$_2$NO, which can be further decomposed to N$_2$ and H$_2$O [46–48].

To further determine the reaction mechanism of NH$_3$-SCR, the *in situ* DRIFTS spectra of NH$_3$ and pre-adsorbed NO + O$_2$ on the Mn$_3$O$_4$ and F-Mn$_3$O$_4$-3% catalysts at 100 °C are performed (Fig. 8c-d). For Mn$_3$O$_4$, the adsorbed NO$_2$ at 1625 cm^{-1} is completely converted after introducing NH$_3$ for 10 min, and the monodentate nitrates (1272, 1528 cm^{-1}) decrease slowly and are still incompletely consumed at 30 min, demonstrating that the reactivity of monodentate nitrates is inferior. The bidentate nitrates at 1548 cm^{-1} are redshifted to 1531 cm^{-1} with increasing reaction time and are completely consumed at 20 min. At the same time, NH$_3$ adsorbed at the Lewis acid site appears at 1603 cm^{-1}. In addition, the intermediate (M-O-NO$_2$-NH$_3$) is also detected at 1443 cm^{-1}. Compared to Mn$_3$O$_4$, the adsorbed NO$_2$ at 1625 cm^{-1} completely disappears after NH$_3$ is introduced for 3 min, and the monodentate nitrates at 1273 cm^{-1} are still incompletely consumed at 30 min, but the reactivity is significantly faster than that of Mn$_3$O$_4$, implying that the reactivity of NO$_x$ species can be improved by doping F

into Mn$_3$O$_4$. The intermediate (M-O-NO$_2$-NH$_3$) is also detected at 1443 cm^{-1}, indicating that the M-O-NO$_2$-NH$_3$ is an important reaction intermediate, which provides a guarantee for the NH$_3$-SCR reaction above 180 °C. According to the above analysis, the Langmuir-Hinshelwood (L-H) mechanism also participates in the NH$_3$-SCR reaction on the F-Mn$_3$O$_4$-x catalysts.

Combined with the *in situ* DRIFTS experiments, the NH$_3$-SCR reaction follows both the E-R and the L-H mechanisms on the surface of the F-Mn$_3$O$_4$-x catalysts. However, the E-R mechanism is the dominant pathway because of the poor reactivity of the adsorbed NO$_x$ species. The reaction pathway of NH$_3$-SCR can be described in the following steps (Eqs. 1–8). In the E-R pathway, gaseous NH$_3$ is first adsorbed on the Lewis acid site to form NH$_{3(ad)}$ (Eq. 1), which can be dissociated into NH$_{2(ad)}$ species (Eq. 2) by dehydrogenation at the adjacent atom, and the NH$_{2(ad)}$ species can react with NO to the form the intermediate of NH$_2$NO (Eq. 3), which can be rapidly decomposed to N$_2$ and H$_2$O (Eq. 4), and form a Brønsted acid site (OH). In the next L-H pathway, gaseous NH$_3$ is absorbed in the Brønsted acid site to form NH$_4^+$ (Eq. 5). Meanwhile, the gaseous NO is adsorbed and oxidized to adsorbed NO$_2$ species (Eq. 6), which can react with NH$_4^+$ to form N$_2$ and H$_2$O, accompanied by the formation of OH (Eq. 7). Finally, the O$_2$ molecule reacts with the OH to generate H$_2$O, restoring the catalyst surface (Eq. 8).

$$NH_{3(g)} + Mn^{3+} \rightarrow Mn^{3+}\text{-}NH_{3(ad)} \tag{1}$$

$$Mn^{3+}\text{-}NH_{3(ad)} + Mn^{3+}=O \rightarrow Mn^{3+}\text{-}NH_{2(ad)} + Mn^{2+}\text{-}OH \tag{2}$$

$$\text{-}NH_2 + NO(g) \rightarrow NH_2NO_{(ad)} \tag{3}$$

$$NH_2NO_{(ad)} \rightarrow N_2 + H_2O \tag{4}$$

$$NH_{3(g)} + Mn^{2+}\text{-}OH \rightarrow Mn^{2+}\text{-}O\text{-}NH_{4(ad)}^+ \qquad (5)$$

$$NO_{(g)} + Mn^{3+}=O \rightarrow O=Mn^{3+}\text{-}NO_{(ad)} \rightarrow Mn^{2+}\text{-}NO_{2(ad)} \qquad (6)$$

$$Mn^{2+}\text{-}NO_{2(ad)} + Mn^{2+}\text{-}O\text{-}NH_{4(ad)}^+ \rightarrow Mn^{2+}\text{-}NO_2\text{-}NH_{3(ad)} + Mn^{2+}\text{-}OH \rightarrow 2$$
$$Mn^{2+}\text{-}OH + N_2 + H_2O \qquad (7)$$

$$4Mn^{2+}\text{-}OH + O_2 \rightarrow 4Mn^{3+}=O + 2 H_2O \qquad (8)$$
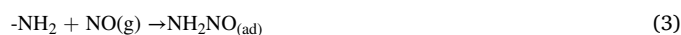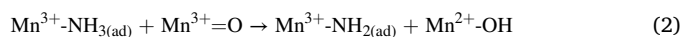
In addition, metal Mn as a transition metal has a good single-electron transfer ability, thus F-Mn$_3$O$_4$-x catalysts follow a single-electron transfer reaction mechanism in the NH$_3$-SCR reaction [49,50]. Our previous studies have demonstrated that NO can react with lattice oxygen on the surface of Mn$_3$O$_4$ to form NO$_2$, accompanied by the reduction of Mn^{3+} to Mn^{2+} [5]. In this cycle, the Mn^{2+} species can be oxidized by O$_2$ to regenerate Mn^{3+}.

4. Conclusion

In summary, we propose a novel *in situ* construction method of F-doped Mn$_3$O$_4$ spinel catalysts through a crystallization-pyrolysis-oxidation strategy. The obtained F-Mn$_3$O$_4$-3 % exhibits a robust catalytic performance with a NO conversion above 90 % from 150° to 310°C at an ultra-high GHSV of 400,000 h^{-1}. The SO$_2$ resistance is also significantly improved compared to pure Mn$_3$O$_4$. Doping of Mn$_3$O$_4$ with F increases the surface acidity and tunes the electronic properties of the catalysts. The increase of acid sites not only facilitates the adsorption of NH$_3$ species, thereby improving NH$_3$-SCR activity, but also inhibits SO$_2$ adsorption on the catalyst surface. The electron conduction between SO$_2$ and Mn^{3+} can be effectively inhibited after F replaces O, resulting in the F-doped Mn$_3$O$_4$ catalysts can selectively oxidizing NO to NO$_2$ rather than oxidizing SO$_2$ to SO$_3$, thereby causing the decrease of sulfate species. Combined with *in situ* DRIFTS experiments, the reaction mechanism of the F-doped Mn$_3$O$_4$ catalyst is proposed, and the NH$_3$-SCR follows both the E-R and L-H mechanisms, with the E-R mechanism being the dominant pathway. Our work provides a novel idea and approach for the design and modulation of SCR catalysts with high activity and SO$_2$ resistance.

CRediT authorship contribution statement

Chong Chen: Conceptualization, Formal analysis, Investigation, Writing – review & editing, Writing – original draft. **Yunxia Wang:** Formal analysis. **Junxi Li:** Formal analysis. **Fengyu Tian:** Formal analysis. **Weijuan Chen:** Formal analysis. **Chao Feng:** Writing – review & editing. **Yuan Pan:** Conceptualization, Writing – review & editing. **Yunqi Liu:** Project administration, Funding acquisition.

Declaration of Competing Interest

The authors declare that they have no known competing financial interests or personal relationships that could have appeared to influence the work reported in this paper.

Data availability

Data will be made available on request.

Acknowledgement

Appendix A. Supporting information

Supplementary data associated with this article can be found in the online version at doi:10.1016/j.apcatb.2023.123086.

References

[1] L.P. Han, S.X. Cai, M. Gao, J.Y. Hasegawa, P.L. Wang, J.P. Zhang, L.Y. Shi, D. S. Zhang, Selective catalytic reduction of NO$_x$ with NH$_3$ by using novel catalysts: state of the art and future prospects, Chem. Rev. 119 (2019) 10916–10976.

[2] Y. Inomata, H. Kubota, S. Hata, E. Kiyonaga, K. Morita, K. Yoshida, N. Sakaguchi, T. Toyao, K.I. Shimizu, S. Ishikawa, W. Ueda, M. Haruta, T. Murayama, Bulk tungsten-substituted vanadium oxide for low-temperature NO$_x$ removal in the presence of water, Nat. Commun. 12 (2021) 557.

[3] M.H. Zhu, J.K. Lai, U. Tumuluri, Z.L. Wu, I.E. Wachs, Nature of active sites and surface intermediates during SCR of NO with NH$_3$ by supported V$_2$O$_5$-WO$_3$/TiO$_2$ catalysts, J. Am. Chem. Soc. 139 (2017) 15624–15627.

[4] Z. Liu, M.M. Wang, S.J. Liu, Z. Chen, L.Z. Yang, K.A. Sun, Y.J. Chen, L.Y. Zeng, W. H. Wang, J.C. Zhao, G.X. Sun, B. Liu, Y. Pan, Y.Q. Liu, C.G. Liu, Design of assembled composite of Mn$_3$O$_4$@Graphitic carbon porous nano-dandelions: a catalyst for Low–temperature selective catalytic reduction of NO$_x$ with remarkable SO$_2$ resistance, Appl. Catal. B Environ. 269 (2020), 118731.

[5] Z. Liu, G.X. Sun, C. Chen, K.A. Sun, L.Y. Zeng, L.Z. Yang, Y.J. Chen, W.H. Wang, B. Liu, Y.K. Lu, Y. Pan, Y.Q. Liu, C.G. Liu, Fe-doped Mn$_3$O$_4$ spinel nanoparticles with highly exposed Fe$_{oct}$–O–Mn$_{tet}$ sites for efficient selective catalytic reduction (SCR) of NO with ammonia at low temperatures, ACS Catal. 10 (2020) 6803–6809.

[6] Xu, Q.; Fang, Z.L.; Chen, Y.Y.; Guo, Y.L.; Guo, Y.; Wang, L.; Wang, Y.S.; Zhang, J.S.; Zhan, W.C. Titania-Samarium-Manganese Composite Oxide for the Low-Temperature Selective Catalytic Reduction of NO with NH3, Environ. Sci. Technol., 54, (2020) 2530–2538.

[7] R.N. Yang, S.M. Peng, B. Lan, M. Sun, Z.H. Zhou, C.Y. Sun, Z.H. Gao, G.C. Xing, L. Yu, Oxygen defect engineering of beta-MnO$_2$ catalysts via phase transformation for selective catalytic reduction of NO, Small 17 (2021), e2102408.

[8] Z. Liu, C. Chen, J.C. Zhao, L.Z. Yang, K.A. Sun, L.Y. Zeng, Y. Pan, Y.Q. Liu, C.G. Liu, Study on the NO$_2$ production pathways and the role of NO$_2$ in fast selective catalytic reduction DeNO$_x$ at low-temperature over MnO$_x$/TiO$_2$ catalyst, Chem. Eng. J. 379 (2020), 122288.

[9] K.L. Song, K.Y. Guo, S.M. Mao, D.D. Ma, Y.X. Lv, C. He, H.K. Wang, Y.H. Cheng, J. W. Shi, Insight into the origin of excellent SO$_2$ tolerance and de-NO$_x$ Performance of quasi-Mn-BTC in the low-temperature catalytic reduction of nitrogen oxide, ACS Catal. 13 (2023) 5020–5032.

[10] Y.L. Li, H. Chen, L. Chen, Y.Y. Zhang, Y.Y. Mi, M.Y. Liao, W.M. Liu, D.S. Wu, Z. G. Li, H.G. Peng, Ternary MnCoVO$_x$ catalysts with remarkable deNO$_x$ performance: dual acid-redox sites control strategy, Appl. Catal. B Environ. 318 (2022), 121779.

[11] C.Z. Sun, H. Liu, W. Chen, D.Z. Chen, S.H. Yu, A.N. Liu, L. Dong, S. Feng, Insights into the Sm/Zr co-doping effects on N$_2$ selectivity and SO$_2$ resistance of a MnO$_x$-TiO$_2$ catalyst for the NH$_3$-SCR reaction, Chem. Eng. J. 347 (2018) 27–40.

[12] T. Lee, H. Bai, Metal sulfate poisoning effects over MnFe/TiO$_2$ for selective catalytic reduction of NO by NH$_3$ at low temperature, Ind. Eng. Chem. Res. 57 (2018) 4848–4858.

[13] X. Fang, Y.J. Liu, Y. Cheng, W.L. Cen, Mechanism of Ce-modified birnessite-MnO$_2$ in promoting SO$_2$ poisoning resistance for low-temperature NH$_3$-SCR, ACS Catal. 11 (2021) 4125–4135.

[14] Y.X. Yu, W. Tan, D.Q. An, X.W. Wang, A.N. Liu, W.X. Zou, C.J. Tang, C.Y. Ge, Q. Tong, J.F. Sun, L. Dong, Insight into the SO$_2$ resistance mechanism on γ-Fe$_2$O$_3$ catalyst in NH$_3$-SCR reaction: a collaborated experimental and DFT study, Appl. Catal. B Environ. 281 (2021), 119544.

[15] T. Zhang, H. Li, Z. Yang, F.R. Cao, L. Li, H.J. Chen, H. Liu, K. Xiong, J. Wu, Z. L. Hong, W.C. Wang, Electrospun YMn$_2$O$_5$ nanofibers: a highly catalytic activity for NO oxidation, Appl. Catal. B Environ. 247 (2019) 133–141.

[16] W. Na, J. Jun, J.W. Park, G. Lee, J. Jang, Highly porous carbon nanofibers co-doped with fluorine and nitrogen for outstanding supercapacitor performance, J. Mater. Chem. A 5 (2017) 17379–17387.

[17] C.L. Wang, S.Q. Wei, F. Li, X.F. Long, T. Wang, P. Wang, S.W. Li, J.T. Ma, J. Jin, Activating a hematite nanorod photoanode via fluorine-doping and surface fluorination for enhanced oxygen evolution reaction, Nanoscale 12 (2020) 3259–3266.

[18] X.J. Li, Y.C. Tang, J.X. Zhu, H.M. Lv, L.M. Zhao, W.L. Wang, C.Y. Zhi, H.F. Li, Boosting the cycling stability of aqueous flexible Zn batteries via F doping in nickel-cobalt carbonate hydroxide cathode, Small 16 (2020), e2001935.

[19] J.F. Xie, W.W. Liu, J.P. Xin, F.C. Lei, L. Gao, H.C. Qu, X.D. Zhang, Y. Xie, Dual effect in fluorine-doped hematite nanocrystals for efficient water oxidation, ChemSusChem 10 (2017) 4465–4471.

[20] M. Díaz-Sánchez, I. Hernández-Benítez, D. Díaz-García, S. Prashar, S. Gómez-Ruiz, Nanohybrids based on F-doped titanium dioxides and carbon species with enhanced dual adsorption-photodegradation activity for water decontamination, Catal. Commun. 169 (2022), 106477.

[21] W.G. Cui, Y.T. Li, H. Zhang, Z.C. Wei, B.H. Gao, J.J. Dai, T.L. Hu, In situ encapsulated Co/MnO$_x$ nanoparticles inside quasi-MOF-74 for the higher alcohols synthesis from syngas, Appl. Catal. B Environ. 278 (2020), 119262.

[22] W.G. Cui, X.Y. Zhuang, Y.T. Li, H. Zhang, J.J. Dai, L. Zhou, Z. Hu, T.L. Hu, Engineering Co/MnO heterointerface inside porous graphitic carbon for boosting the low-temperature CO₂ methanation, Appl. Catal. B Environ. 287 (2021), 119959.

[23] S.L. Zhao, C.H. Tan, C.T. He, P.F. An, F. Xie, S. Jiang, Y.F. Zhu, K.H. Wu, B. W. Zhang, H.J. Li, J. Zhang, Y. Chen, S.Q. Liu, J.C. Dong, Z.Y. Tang, Structural transformation of highly active metal–organic framework electrocatalysts during the oxygen evolution reaction, Nat. Energy 5 (2020) 881–890.

[24] C. Chen, C. Feng, Y.X. Wang, J.X. Li, Z. Liu, W.H. Wang, Y. Pan, Y.Q. Liu, Design of robust Co-doped Mn₃O₄ spinel catalysts for selective catalytic reduction of NO with NH₃ at low temperatures, Appl. Surf. Sci. 602 (2022) 154384.

[25] C. Feng, Q.Q. Gao, G.Y. Xiong, Y.F. Chen, Y. Pan, Z.Y. Fei, Y.P. Li, Y.K. Lu, C.G. Liu, Y.Q. Liu, Defect engineering technique for the fabrication of LaCoO₃ perovskite catalyst via urea treatment for total oxidation of propane, Appl. Catal. B Environ. 304 (2022), 121005.

[26] C. Feng, F. Jiang, G.Y. Xiong, C. Chen, Z. Wang, Y. Pan, Z.Y. Fei, Y.K. Lu, X.B. Li, R. D. Zhang, Y.Q. Liu, Revelation of Mn⁴⁺-Oₛᵤᵣ-Mn³⁺ active site and combined Langmuir-Hinshelwood mechanism in propane total oxidation at low temperature over MnO₂, Chem. Eng. J. 451 (2023), 129968.

[27] J. Ji, X.L. Lu, C. Chen, M. He, H.B. Huang, Potassium-modulated δ-MnO2 as robust catalysts for formaldehyde oxidation at room temperature, Appl. Catal. B Environ. 260 (2020), 118210.

[28] S.C. Xiong, Y. Peng, D. Wang, N. Huang, Q.F. Zhang, S.J. Yang, J.J. Chen, J.H. Li, The role of the Cu dopant on a Mn₃O₄ spinel SCR catalyst: improvement of low-temperature activity and sulfur resistance, Chem. Eng. J. 387 (2020), 124090.

[29] H. Pan, Y.F. Jian, C.W. Chen, C. He, Z. Hao, Z.P. Shen, H.X. Liu, Sphere-shaped Mn₃O₄ catalyst with remarkable low-temperature activity for methyl-ethyl-ketone combustion, Environ. Sci. Technol. 51 (2017) 6288–6297.

[30] G. Ou, Y.S. Xu, B. Wen, R. Lin, B.H. Ge, Y. Tang, Y.W. Liang, C. Yang, K. Huang, D. Zu, R. Yu, W.X. Chen, J. Li, H. Wu, L.M. Liu, Y.D. Li, Tuning defects in oxides at room temperature by lithium reduction, Nat. Commun. 9 (2018) 1302.

[31] J. Fu, F.M. Hassan, C. Zhong, J. Lu, H. Liu, A.P. Yu, Z.W. Chen, Defect engineering of chalcogen-tailored oxygen electrocatalysts for rechargeable quasi-solid-state zinc-air batteries, Adv. Mater. 29 (2017), 1702526.

[32] S.P. Mo, Q. Zhang, J.Q. Li, Y.H. Sun, Q.M. Ren, S.B. Zou, Q. Zhang, J.H. Lu, M. L. Fu, D.Q. Mo, J.L. Wu, H.M. Huang, D.Q. Ye, Highly efficient mesoporous MnO2 catalysts for the total toluene oxidation: Oxygen-Vacancy defect engineering and involved intermediates using in situ DRIFTS, Appl. Catal. B Environ. 264 (2020), 118464.

[33] H. Jiang, Z.X. Wei, L. Ma, Y.F. Yuan, J.J. Hong, X.Y. Wu, D.P. Leonard, J. Holoubek, J.J. Razink, W.F. Stickle, F. Du, T.P. Wu, J. Lu, X.L. Ji, An aqueous dual-ion battery cathode of Mn₃O₄ via reversible insertion of nitrate, Angew. Chem. Int. Ed. Engl. 58 (2019) 5286–5291.

[34] S.H. Chen, Z.P. Su, H. Wang, P.C. Sun, T.H. Chen, Lattice distortion in Mn₃O₄/SmOₓ nanocomposite catalyst for enhanced carbon monoxide oxidation, Chem. Eng. J. 451 (2023), 138635.

[35] Q. Zhao, B.B. Chen, J. Li, X.B. Wang, M. Crocker, C. Shi, nsights into the structure-activity relationships of highly efficient CoMn oxides for the low temperature NH3-SCR of NOx, Appl. Catal. B Environ. 277 (2020), 119215.

[36] N.Q. Zhang, L.C. Li, Y.Z. Guo, J.D. He, R. Wu, L.Y. Song, G.Z. Zhang, J.S. Zhao, D. S. Wang, H. He, A MnO2-based catalyst with H2O resistance for NH3-SCR: study of catalytic activity and reactants-H2O competitive adsorption, Appl. Catal. B Environ. 270 (2020), 118860.

[37] B. Wang, M.X. Wang, L.N. Han, Y.Q. Hou, W.R. Bao, C.M. Zhang, G. Feng, L. P. Chang, Z.G. Huang, J.C. Wang, Improved activity and SO₂ resistance by Sm-modulated redox of MnCeSmTiOₓ mesoporous amorphous oxides for low-temperature NH₃-SCR of NO, ACS Catal. 10 (2020) 9034–9045.

[38] G. Li, B.D. Wang, Z.R. Ma, H.Y. Wang, J. Ma, C.L. Zhao, J.L. Zhou, D.H. Lin, F. Q. He, Z.H. Han, Q. Sun, Y. Wang, Aluminium-induced component engineering of mesoporous composite materials for low-temperature NH₃-SCR, Commun. Chem. 3 (2020) 66.

[39] J.J. Liu, G.Z. He, W.P. Shan, Y.B. Yu, Y.L. Huo, Y. Zhang, M. Wang, R. Yu, S.S. Liu, H. He, Introducing tin to develop ternary metal oxides with excellent hydrothermal stability for NH3 selective catalytic reduction of NO, Appl. Catal. B Environ. 291 (2021), 120125.

[40] K. Liu, H. He, B.W. Chu, Microkinetic study of NO oxidation, standard and fast NH₃-SCR on CeWOₓ at low temperatures, Chem. Eng. J. 423 (2021), 130128.

[41] Chen, R.Y.; Fang, X.Y.; Li, J.H.; Zhang, Y.; Liu, Z.M. Mechanistic investigation of the enhanced SO2 resistance of Co-modified MnOx catalyst for the selective catalytic reduction of NOx by NH3, Chem. Eng. J., 452, (2023) 139207.

[42] Z.C. Chen, S. Ren, M.M. Wang, J. Yang, L. Chen, W.Z. Liu, Q.C. Liu, B.X. Su, Insights into samarium doping effects on catalytic activity and SO₂ tolerance of MnFeOₓ catalyst for low-temperature NH₃-SCR reaction, Fuel 321 (2022), 124113.

[43] Y. Xin, H. Li, N.N. Zhang, Q. Li, Z.L. Zhang, X.M. Cao, P. Hu, L.R. Zheng, J. A. Anderson, Molecular-level insight into selective catalytic reduction of NOₓ with NH₃ to N₂ over a highly efficient bifunctional Vₐ-MnOₓ catalyst at low temperature, ACS Catal. 8 (2018) 4937–4949.

[44] X.S. Liu, Q.F. Yu, H.F. Chen, P. Jiang, J.F. Li, Z.Y. Shen, The promoting effect of S-doping on the NH₃-SCR performance of MnOₓ/TiO₂ catalyst, Appl. Surf. Sci. 508 (2020), 144694.

[45] L.J. Yan, Y.Y. Ji, P.L. Wang, C. Feng, L.P. Han, H.R. Li, T.T. Yan, L.Y. Shi, D. Zhang, Alkali and phosphorus resistant zeolite-like catalysts for NOx Reduction by NH₃, Environ. Sci. Technol. 54 (2020) 9132–9141.

[46] J.C. Mu, X.Y. Li, W.B. Sun, S.Y. Fan, X.Y. Wang, L. Wang, M.C. Qin, G.Q. Gan, Z. F. Yin, D.K. Zhang, Inductive effect boosting catalytic performance of advanced Fe₁₋ₓVₓOₐ catalysts in low-temperature nh3 selective catalytic reduction: insight into the structure, interaction, and mechanisms, ACS Catal. 8 (2018) 6760–6774.

[47] Zhu, M.H.; Lai, J.K.; Tumuluri, U.; Ford, M.E.; Wu, Z.L.; Wachs, I.E. Reaction pathways and kinetics for selective catalytic reduction (SCR) of acidic NOx emissions from power plants with NH3, ACS Catal., 7, (2017) 8358–8361.

[48] H. Wang, Z.P. Qu, S.C. Dong, C. Tang, Mechanism study of FeW mixed oxides to the selective catalytic reduction of NO with NH₃: in situ DRIFTS and MS, Catal. Today 307 (2018) 35–40.

[49] Y. Chen, C. Chen, Y.H. Liu, L. Yu, Probing the effect of nitrate anion in CAN: an additional opportunity to reduce the catalyst loading for aerobic oxidations, Chin. Chem. Lett. (2023), 108489.

[50] X.Y. Dong, Z.L. Li, Q.S. Gu, X.Y. Liu, Ligand development for copper-catalyzed enantioconvergent radical cross-coupling of racemic alkyl halides, J. Am. Chem. Soc. 144 (2022) 17319–17329.